J. Ocean Univ. China (Oceanic and Coastal Sea Research)
https://doi.org/10.1007/s11802-019-3875-9
ISSN 1672-5182, 2019 18 (3): 542-552
http://www.ouc.edu.cn/xbywb/
E-mail:xbywb@ouc.edu.cn

Improvements in Long-Lead Prediction of Early-Summer Subtropical Frontal Rainfall Based on Arctic Sea Ice

XING Wen[1), 2)], and HUANG Fei[1), 2), 3), *]

1) *Key Laboratory of Physical Oceanography, Ocean University of China, Qingdao* 266100, *China*
2) *Laboratory for Ocean and Climate Dynamics, Pilot National Laboratory for Marine Science and Technology (Qingdao), Qingdao* 266100, *China*
3) *Ningbo Collaborative Innovation Center of Nonlinear Harzard System of Ocean and Atmosphere, Ningbo University, Ningbo* 315211, *China*

(Received April 1, 2018; revised March 7, 2019; accepted March 25, 2019)

Abstract Seasonal prediction of East Asia (EA) summer rainfall, especially with a longer-lead time, is in great demand, but still very challenging. The present study aims to make long-lead prediction of EA subtropical frontal rainfall (SFR) during early summer (May–June mean, MJ) by considering Arctic sea ice (ASI) variability as a new potential predictor. A MJ SFR index (SFRI), the leading principle component of the empirical orthogonal function (EOF) analysis applied to the MJ precipitation anomaly over EA, is defined as the predictand. Analysis of 38-year observations (1979–2016) revealed three physically consequential predictors. A stronger SFRI is preceded by dipolar ASI anomaly in the previous autumn, a sea level pressure (SLP) dipole in the Eurasian continent, and a sea surface temperature anomaly tripole pattern in the tropical Pacific in the previous winter. These precursors foreshadow an enhanced Okhotsk High, lower local SLP over EA, and a strengthened western Pacific subtropical high. These factors are controlling circulation features for a positive SFRI. A physical-empirical model was established to predict SFRI by combining the three predictors. Hindcasting was performed for the 1979–2016 period, which showed a hindcast prediction skill that was, unexpectedly, substantially higher than that of a four-dynamical models' ensemble prediction for the 1979–2010 period (0.72 *versus* 0.47). Note that ASI variation is a new predictor compared with signals originating from the tropics to mid-latitudes. The long-lead hindcast skill was notably lower without the ASI signals included, implying the high practical value of ASI variation in terms of long-lead seasonal prediction of MJ EA rainfall.

Key words East Asia subtropical frontal rainfall; long-lead seasonal prediction; Arctic sea ice; Physical-empirical model

1 Introduction

East Asia (EA) is vulnerable to summertime droughts and floods, which frequently cause devastating agricultural and economic losses (Tao and Chen, 1987; Yuan *et al*., 2008a, b; Gu *et al*., 2009a, b). The losses arising from climate-related disasters have notably increased in recent years due to the economic boom. The life- threatening impact of droughts and floods on the dense population centers of EA has incentivized numerous scientists to investigate the causes and predictability of the East Asia summer monsoon (EASM) rainfall variations. One of the difficulties in EASM prediction is linked to prominent seasonal migration of the subtropical monsoon rain band from May to August (Tao and Chen, 1987; Wang and Ho, 2002). Studies have shown that the May and June (MJ)/July and August (JA) rainfall patterns are similar. However, pronounced differences exist between early summer (MJ) and peak summer (JA) precipitation (Wang *et al*., 2009; Li and Zhou, 2011; Su *et al*., 2014; Oh and Ha, 2015). It has been proved by a series of studies that EASM prediction is beneficial when making MJ and JA summer predictions separately (Xing *et al*., 2016; Yim *et al*., 2016; Xing and Wang, 2017). This study addresses early-summer precipitation variability.

The observed long-term mean precipitation in MJ is characterized by a prominent rain band extending about 9000 km from the Bay of Bengal northeastward via Indochina, Southern China all the way to east of Japan. This prominent rain band is associated with the EA subtropical front (Tao and Chen, 1987), which is a defining feature of the Asian monsoon and produces the most prominent precipitation band in the global subtropics. This period involves the onset of the EASM over the South China Sea in mid-May, the Meiyu onset over China, and the Baiu onset in South Japan in early and mid-June. In MJ, Indo-China, Southern China, Taiwan, and Okinawa all reach their yearly peak or one of their peaks in the local rainy seasons (Chen, 1983; Yim *et al*., 2014). Therefore, predicting the MJ subtropical frontal rainfall (SFR) is important for agricultural planning and water resource man-

* Corresponding author. E-mail: huangf@ouc.edu.cn

agement in these regions. Xing *et al.* (2017) has made a 0-month lead objective prediction of anomalous MJ EA precipitation spatial structure using an alternative, empirical orthogonal function (EOF)-based physical-empirical (P-E) model approach. In a practical forecast, a sufficient lead time is needed to make timely management decisions. Therefore, long-lead seasonal prediction is in great demand. However, the prediction would be difficult and the skills would decrease with increasing lead time using the precursors originated from the tropics to mid-latitudes (Wang *et al*., 2008; Lee *et al*., 2011; Xing *et al.*, 2017). Identifying additional potential sources of predictors, especially from the polar regions, may be helpful in skillfully predicting MJ EA SFR at a longer-lead time.

In recent decades, an increasing number of studies have postulated that Arctic sea ice (ASI) variability plays a crucial role in affecting global atmospheric circulation and modulating regional weather or climate (*e.g*., Alexander *et al*., 2004; Magnusdottir *et al*., 2004; Singarayer *et al*., 2006; Deser *et al*., 2004, 2010; Holland *et al*., 2006; Serreze *et al*., 2007; Wang and Overland, 2009; Kumar *et al*., 2010; Li and Wu, 2012; Zhang and Li, 2016; and many others). The role of ASI in the EA climate system has been extensively investigated using observations and simulations. For instance, Zuo *et al*. (2016) suggested that autumn ASI anomalies may affect winter temperature in China through modulating the Siberian High. Numerical results from Wu *et al.* (2011) indicated that anomalous ASI can lead to an anomalous blocking high over the northern Eurasian continent in winter and in turn influences the EA winter monsoon. Reduced ASI the previous winter may favor rich spring precipitation over EA by exciting downstream teleconnections with a distinct Rossby wave train prevailing over the Eurasian continent (Wu *et al*. 2016). Wu *et al.* (2009b) found that spring ASI corresponded to anomalous China summer rainfall through a south-north dipole structure over EA south to Lake Baikal. Therefore, we can conclude that ASI has a crucial contribution to seasonal prediction of EA climate. However, in different seasons, the effects and the corresponding physical mechanisms may vary. It is still not clear how ASI affects variations in MJ SFR and to what extent it contributes to the MJ EA rainfall prediction.

The present work attempts to consider ASI as a potential predictor and translate its signals into useful prediction tools. Also, a long-lead prediction model is established to predict MJ SFR using ASI anomalies along with signals from the tropical to mid-latitude regions. In Section 2, we describe the data sets and the method used in this study. The distinctive rainfall and circulation structures of an enhanced MJ subtropical front are briefly described in Section 3 as background information. The statistical relationship of each predictor with MJ subtropical fronts and their associated physical effects are presented in Section 4. In Section 5, a long-lead P-E model is established to forecast the strength of the MJ SFR, and a hindcast is performed for the 1979–2016 period. Section 6 summaries the main conclusions and discusses some outstanding issues.

2 Data and Methods

2.1 Data

The main datasets employed in this study include 1) monthly mean precipitation data from the Global Precipitation Climatology Project (GPCP, v2.3) datasets (Huffman *et al*., 2011); 2) monthly mean SST from NOAA Extended Reconstructed SST (ERSST v4, Huang *et al*., 2015; Liu *et al*., 2015); 3) monthly mean atmospheric fields, taken from ERA-interim (Dee *et al*., 2011); 4) sea ice concentration (SIC) data from the Hadley Center Sea Ice and Sea Surface Temperature datasets (HadISST, Rayner *et al*., 2003).

The data period chosen in this study is 1979 to 2016, since there was a prominent decadal shift in the late 1970s, which has caused significant changes in the EASM-ENSO relationship (Wu and Wang, 2002; Zhou *et al*., 2009; Yun *et al*., 2010). Focusing on the recent 38 years can partially avoid the complexity arising from multi-decadal impacts on year-to-year variations. Early-summer rainfall anomalies are calculated from the deviation of MJ mean rainfall from the 38-year climatology (1979–2016).

2.2 Method

A P-E prediction model was established to predict MJ SFR. Selection of physically meaningful predictors was at the heart of the P-E model. More specifically, we emphasized understanding of the physical processes that explain the lead-lag relationships between the predictors and the predictand in the selection of predictors. Statistical tests were used as an auxiliary tool to maximize the predictors-predictand correlation in training periods, to confirm their significance, and ascertain mutual independence among the predictors (Wang *et al*., 2015b). This means that those predictors should have been relatively independent in their physical meanings and should have avoided those predictors that were well-correlated.

The P-E model has been applied to predict Asia summer rainfall (Li and Wang, 2016; Xing *et al*., 2016; Yim *et al*., 2016), summer rainfall over northwest China (Xing and Wang, 2017), and other climate variability (*e.g*., Lee *et al*., 2013; Wang *et al*., 2013). These studies all concluded that the P-E prediction model is a useful approach for seasonal prediction compared with the current dynamical models, especially over subtropical to mid-latitude regions.

Stepwise regression was used to establish the P-E model. Prior to regression, all variables were normalized by removing their means and dividing by their corresponding standard deviation, which allowed direct comparison of the relative contribution of each predictor by examining the normalized regression coefficient.

Stepwise regression identifies the ‘most desirable’ predictors at each step. Each selected predictor had a significant contribution to increasing the regressed variance by a standard F-test (Panofsky and Brier, 1968). A 95% statistical significance level was used as a criterion to select new predictors at each step. Once selected into the model,

a predictor can only be removed if its significance level falls below 95% by the addition/removal of another variable. To circumvent overfitting, the number of predictors was required to be less than or equal to 4 (*i.e.*, about 10% of the sample size of 38).

A cross-validation method (Michaelsen, 1987) was used to make a retrospective forecast. To lessen the overfitting problem, we left out three years of data progressively centered on a forecast target year for the period of 1979–2016, then trained the model by using the data of the remaining years and finally applied the model to forecast the three target years.

3 Interannual Variability of Subtropical Frontal Rainfall in Early Summer

3.1 An Index that Measures the Strength of Subtropical Frontal Rainfall

To facilitate the study of the interannual variation and prediction of the MJ SFR, an EOF analysis was applied to the MJ mean precipitation anomaly over EA (20˚N–45˚N, 100˚E–130˚E). The leading mode accounted for 26.0% of the total interannual variance. According to the rule given by North *et al.* (1982), the leading mode is statistically distinguished from the rest of the eigenvectors in terms of the sampling error bars.

The spatial pattern of the first EOF mode (Fig.1a) showed a north-south dipole pattern with enhanced precipitation over southern China to the East China Sea and dry anomalies over central China and southern Korea. Another weak positive rainfall center was located to the far northeast of China. The time series of the first principal component (PC1) exhibited considerable interannual variations as well as a decadal shift in the early 1990s (Fig.1b). The simultaneous large-scale precipitation anomalies associated with PC1 demonstrated an enhancement of the entire MJ SFR, stretching from southern China to south of Japan compared to the climatological MJ mean precipitation (Fig.3c).

In order to test the robustness of this leading mode, we conducted an EOF analysis of land precipitation for the same EA domain (*i.e.*, the land coverage was the same but no ocean rainfall) during the 56-year period (1960–2015). The results showed that both the spatial patterns and the PCs were extremely similar to those of the leading mode shown in Figs.1a and 1b in spite of different datasets, training period, and analysis domain (one has ocean and the other has no ocean), indicating that the leading mode of MJ EA rainfall is remarkably robust (Figures not shown).

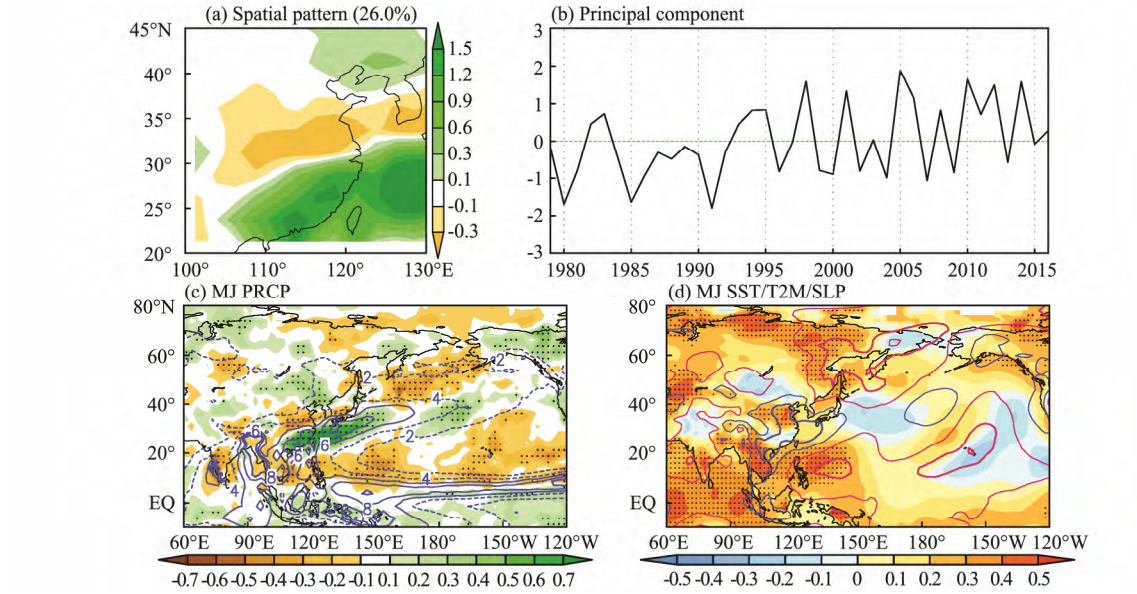

Fig.1 (a) Spatial pattern and (b) corresponding principal component (PC1) of the first EOF mode (EOF1) derived from May–June (MJ) mean precipitation over East Asia (20˚N–45˚N, 100˚E–130˚E) for the period of 1979–2016. (c) MJ precipitation rate (contours in units of mm day^{-1}) averaged for 1979–2016 and the correlation coefficients of anomalous MJ mean precipitation based on PC1 (shading). (d) Correlation maps of anomalous MJ mean SST (shading over ocean)/2 m air temperature over land (T2M, shading over land)/SLP (contours) anomalies based on PC1. Areas exceeding 90% confidence level for rainfall, SST and T2M are dotted in (c) and (d). Red/blue thin contours in (d) indicate positive/negative correlation coefficients of 0.1 and 0.4. Thick contours in (d) represent the correlation coefficient (±0.27) significant at the 90% confidence level for SLP.

Therefore, the leading PC (Fig.1b) was used to measure the intensity of the MJ SFR. A high value of the SFR index (SFRI) was characterized by abundant Meiyu/Baiu frontal rainfall. This index could also tell us the percentage of total variance it accounts for. This piece of information is desirable for any quantitative measure.

3.2 Structure of Rainfall and Circulations Associated with a Strong SFRI

The MJ SFR anomalies have significant interannual variability (Fig.1b). To see what large-scale circulation anomalies affect the rainfall variation, simultaneous cor-

relation maps of the precipitation, SST, 2 m air temperature over land, and SLP anomalies with reference to SFRI are depicted in Figs.1c and 1d.

A positive SFRI was associated with a strong, large-scale anomalous high over the Philippine Sea and the North Pacific implying a strengthened western Pacific subtropical high (WPSH). Cooling SSTs (albeit weak) appeared to the southeast of the WPSH anomaly as the anomalous northeasterly winds strengthened mean easterlies. The Philippine Sea was warmed due to the reduced cloudiness and increased downward solar radiation. Note that the northern Indian Ocean warming is also a result of the subsidence and easterly anomalies associated with the extended anticyclone. In correspondence with the WPSH anomaly, a pronounced rainfall deficit was seen in the western North Pacific (WNP).

To the north of the suppressed rainfall region, abundant moisture was transported toward the EA subtropical monsoon frontal zone along the northwest flank of the anomalous anticyclone, leading to increasing precipitation over southern China and the Meiyu/Baiu band. The enhanced rainfall band was also accompanied by a cyclonic lower SLP anomaly located over eastern China and the coastal areas, which can be seen clearly in Fig.1d.

Another significant characteristic associated with a strong SFRI was that the Okhotsk High pressure was strengthened along with reduced precipitation. Several studies (Ding, 1992; Wang *et al*., 2001) have pointed out that the Okhotsk High is one of the crucial systems in characterizing the Meiyu/Baiu system. To the west of the anomalous high, warm air is transported to northeastern Eurasia along the southerlies, inducing anomalous land warming there. To its east side, the high anomaly brings cold air from the north to meet with warm and moist southwesterlies, enhancing the subtropical frontal rainfall. Note that the regression patterns of 850 hPa and 500 hPa geopotential height with reference to PC1 (Figures not shown) exhibited similar characteristics with the correlation map of SLP (Fig.1d), demonstrating the robustness of the atmospheric circulation anomalies associated with the SFRI.

As a summary of the foregoing, there are three featured circulation systems that are closely related to MJ SFR enhancement: a) anomalous higher SLP over WNP, b) local lower SLP over eastern China, and c) an enhanced Okhotsk High. These features provide illuminating hints for searching for predictors. In the following section, we will choose associated predictors that have physical linkage with these circulation systems.

4 Physical Predictors in Predicting SFRI

The selection of predictors in this study was primarily based on the three circulation characteristics discussed in Section 3.2 and our physical understanding of the lead-lag linkage between the predictand and predictors. Statistical tests and stepwise regression were used as auxiliary tools to verify the statistical significance and relative independence of the selected predictors.

In selecting predictors, we considered SST, SLP, and SIC. SST and SLP, which are in accordance with the meteorological parameters used for predicting EA rainfall during July–August (Xing *et al*., 2016) and various other relative works (Wang *et al*., 2015a; Xing and Wang, 2017), can reflect anomalous lower boundary conditions over the ocean and land surfaces. SIC, representing the ASI variation, is explored in this study as a new potential predictor since the crucial roles of ASI in EA climate variability have been identified by numerous works (Wu *et al*., 2009a; Zuo *et al*., 2016, and many others). The physical processes of SIC, SLP, and SST affecting SFRI variability are discussed in the following subsection. No other circulation anomalies were selected because the seasonal circulation anomalies were driven by interaction with the lower boundary anomalies and have little memory by themselves, except for SLP.

4.1 Arctic Sea Ice Signals

To investigate the relationship between the early-summer SFR and ASI, we calculated the correlation coefficients (CCs) between the SFRI and the bimonthly running mean SIC over the Arctic in the preceding twelve months from the previous July to April of the target year. As shown in Fig.2, significant positive correlation values emerged over the Beaufort Sea expanding to the Greenland Sea during the previous autumn, and persisted into the following spring, reflecting the anomalous variation of multiyear sea ice. Another pronounced feature was the prevalence of significant negative values along the northern edge of the Eurasian continent from the preceding late summer through autumn, then gradually weakening during the following winter and disappearing in spring. It suggests that anomalous sea ice may yield precursory signals for an early-summer SFRI anomaly. The maximum CC of the combination signal appears in October–November (ON), during which period ASI experiences its strongest variation (Fig.2d).

In light of the remarkable correlation with SFRI as well as the higher persistence of this relationship, dipolar Arctic SIC anomalies during the preceding ON mean were selected as one of the predictors of SFRI. The predictor named ARCSIC was defined by the differential SIC anomalies averaged over the Beaufort Sea to the Green-land Sea (75˚N–87.5˚N, 150˚W–0˚) and the northern seaboard of Eurasia (71˚N–78˚N, 60˚E–150˚W) during the previous ON mean (Table 1). This dipole SIC anomaly pattern seemed to interact with Arctic amplification effects.

How can autumnal ASI affect the early-summer subtropical front? To answer this question, we took the predictor ARCSIC as a reference and computed the simultaneous and lag correlations with large-scale circulation fields. The 2 m air temperature anomalies over the Arctic associated with ARCSIC showed pronounced negative values centering over the Beaufort Sea and surrounding areas in the preceding autumn and winter (Figs.3a–3b). This cooling signal was consistent with locally increasing SIC, shown in Figs.2d–2f. The correlated 500 hPa geopotential high field with ARCSIC from autumn through win-

ter showed a positive Arctic Oscillation (AO)-like pattern, *e.g.*, negative pressures in the polar and subpolar regions and positive anomalies over mid-latitude regions (Figs. 3c–3d). The CC between ARCSIC and the simultaneous AO index as defined by Li and Wang (2003a) was 0.39 beyond the 95% confidence level. The 200 hPa westerly jet over high latitudes was strengthened, accompanied by the positive AO pattern.

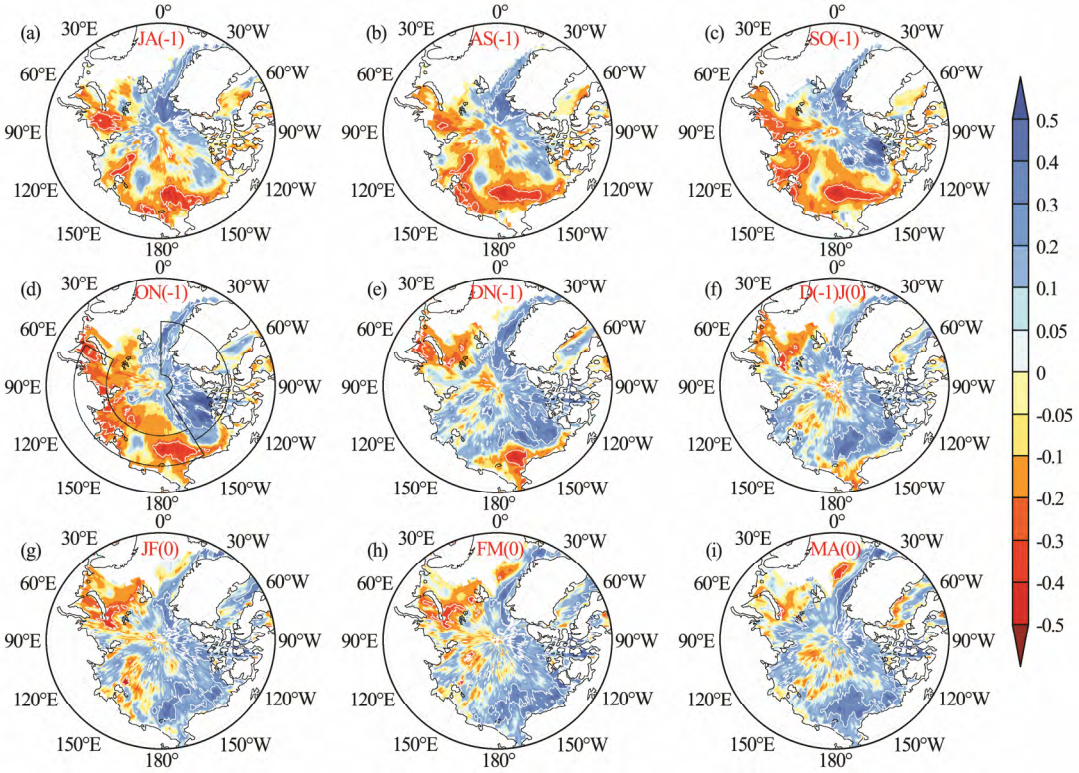

Fig.2 Correlation maps of bimonthly running mean sea ice concentration (SIC) over the Arctic based on PC1. Titles on top of each figure indicate the two-month period. White contours represent the correlation coefficient significant at the 90% confidence level. The sector regions in (d) outline the areas used to define the predictors.

Table 1 Definition of each 3-month lead predictor selected for the prediction of MJ subtropical frontal precipitation variability

Name	Meaning	Definition
ARCSIC	Previous October–November mean dipole SIC anomalies over Arctic	SIC (75˚N–87.5˚N, 150˚W–0˚) − (71˚N–78˚N, 60˚E–150˚W)
EUASLP	Previous December–January mean dipole SLP anomalies over Eurasia	SLP (45˚E–145˚E, 50˚N–80˚N) − (110˚E–135˚E, 20˚N–40˚N)
TPSST	Previous December–January mean SSTA over equatorial Pacific	SST (120˚E–145˚E, 10˚N–25˚N) + (120˚W–80˚W,10˚S–20˚N) − (180˚–140˚W, 10˚N–20˚N)

The AO is a climate mode characterized by winds circulating counterclockwise around the Arctic at around 55˚N latitude. When the AO is in its positive phase, a ring of strong winds circulating around the North Pole acts to confine colder air across polar regions. Therefore, the positive AO corresponds to cooling anomalies over Arctic regions, which was also seen in previous studies (Honda *et al*., 2009; Wu *et al*., 2011; Liu *et al*., 2012). To the contrary, this belt of winds becomes weaker and more distorted in the negative phase of the AO, which allows an easier southward penetration of colder, Arctic air masses.

To the south of the anomalous higher pressure ridge, easterly anomalies appear over northern North Atlantic in autumn and strengthen in winter, favoring a cyclonic shear vorticity (Figs.3c and 3d). Hence, corresponding to the high-latitude pressure anomalies associated with ARCSIC, the North Atlantic displays a resultant dipole pattern of 500 hPa geopotential height anomalies in winter. This dipole pattern shows a barotropic structure so that it can be captured clearly in the correlation map of SLP accompanying a tripole SST pattern (Fig.4a). A SLP and SST anomaly (SSTA) pattern persisted from winter to spring with a slightly northward movement, implying a negative North Atlantic Oscillation (NAO) phase. The CC between ARCSIC and the NAO index as defined by Li and Wang (2003b) during spring is −0.42, which is statistically significant at the 99% confidence level.

The North Atlantic tripole SSTA associated with a NAO negative phase may contribute to the downstream development of subpolar teleconnections across northern Eura-

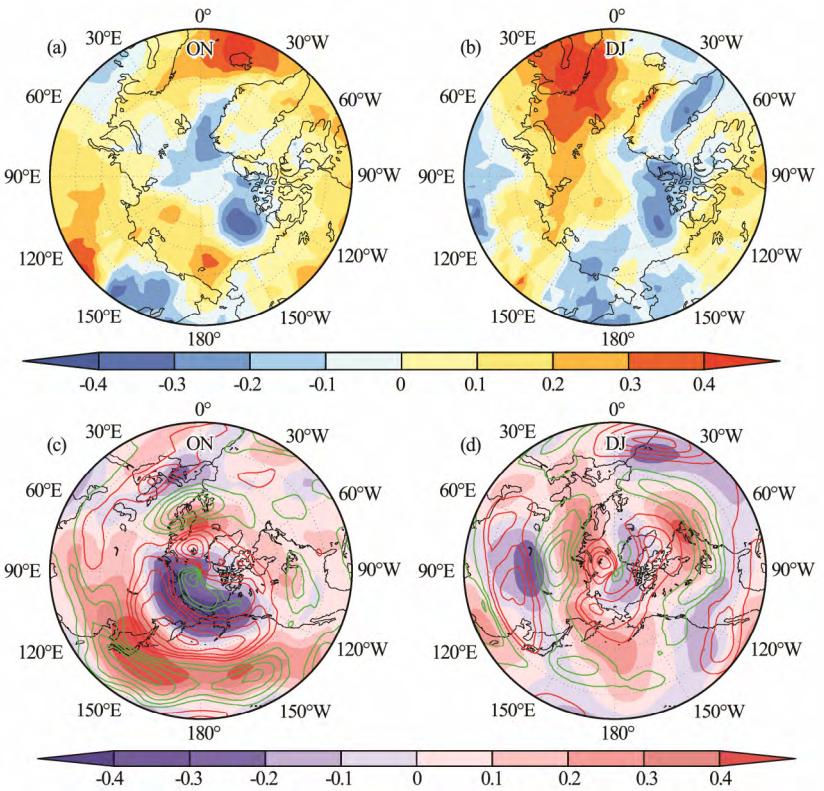

Fig.3 (a–b) Correlation coefficients of the previous October–November (ON) mean, previous December–January (DJ) mean, and 2 m air temperature based on the predictor ARCSIC. (c–d) Same as in (a–b) but for 500 hPa geopotential height (shading) and 200 hPa zonal winds (contours). Red solid contours indicate a positive correlation coefficient between 200 hPa zonal winds and ARCSIC starting from 0.1 with an interval of 0.1. A similar interval applies to the green lines, except for a negative correlation.

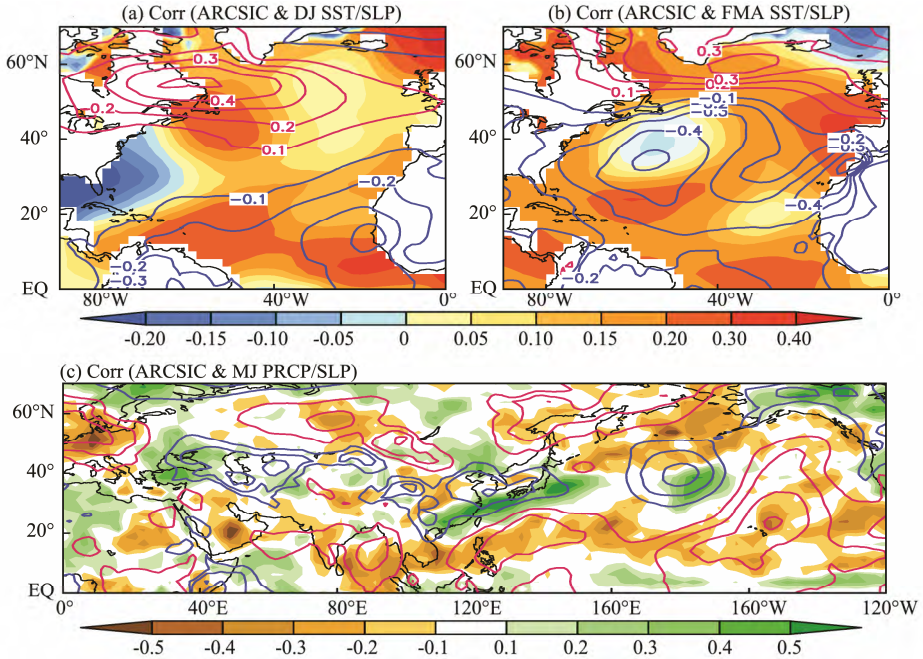

Fig.4 Correlation maps of (a) DJ mean and (b) February–April (FMA) mean SST (shading) and SLP (contour) based on the predictor ARCSIC. (c) Correlation maps of MJ mean precipitation (shading) and SLP (contour) based on ARCSIC. Red solid contours indicate a positive correlation coefficient between SLP and ARCSIC starting from 0.1 with an interval of 0.1. A similar interval applies to the blue lines, except for a negative correlation.

sia, which enhances the high over the Ural Mountain and the Okhotsk Sea (Fig.4c). This process was verified by Wu *et al.* (2009b) in a numerical experiment. As discussed in Section 3.2, enhancement of the Okhotsk High is a key

feature strengthening MJ SFR. Therefore, ARCSIC is a physically meaningful predictor for SFRI prediction, reflecting the role of the Okhotsk High. This predictor only involves information before and during the preceding November. Thus, it is a 5-month lead predictor.

4.2 Precursors from the Tropics and Mid-Latitudes

Since this study focuses on long-lead prediction, all predictors are preferred to be at least three months ahead of May. Analysis of a large number of long-lead correlation maps reveals that the SST and SLP anomalies in the preceding winter season (December–January mean, DJ) have the best indicative signals. Fig.5 displays the correlation maps of SST and SLP anomalies during the DJ mean associated with MJ SFRI, which yielded another two physically meaningful predictors.

The second predictor was the dipole differential SLP anomalies during the DJ mean between northern Eurasia (45˚E–145˚E, 50˚N–80˚N) and the EA region (110˚E–135˚E, 20˚N–40˚N), which is called EUASLP. The dashed rectangular regions outline where the predictor EUASLP is defined (Fig.5).

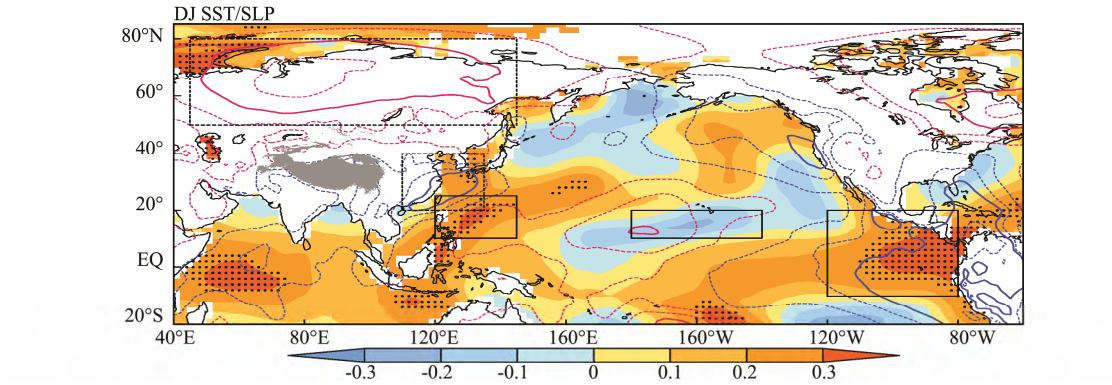

Fig.5 Correlation maps of anomalous DJ mean SST (shading) and SLP (contours) based on the PC1. Areas exceeding 90% confidence level for SST are dotted. Thick contours represent the correlation coefficient significant at the 90% confidence level for SLP. Red dashed contours indicate positive correlation coefficients of 0.1, 0.2, 0.4 and 0.5. A similar interval applies to the blue dashed line, except for a negative correlation. The rectangular regions outline where the predictors are defined.

This predictor corresponded to the large-scale dipole SLP anomaly pattern during winter through spring between the Eurasian continent and the northern Indian Ocean expanding to EA (Figs.6a and 6b). Anomalous westerlies prevailed along the southern flank of the lower SLP. The Indo-Pacific warm pool region warmed up due to the suppressed South Asian winter monsoon. In turn, the warmed SSTA over the tropical western Pacific favored intensive convection activities, inducing enhanced convective precipitation. The wet signals can generate anomalous cyclones to their west on both sides of the equator as a Rossby wave response, enhancing the aforementioned westerly anomalies (Fig.6c). Such an air-sea interactive process helps sustain the negative pressures. Accordingly, local lower SLP anomalies and anomalous cyclones occurred over the South China Sea and southern China, inducing plentiful rainfall there (Fig.6d). Therefore, this predictor corresponded to lower SLP anomalies over eastern China, which was one of the key characteristics that favored a stronger SFRI.

Another significant precursor, shown in Fig.5, was the tripole SSTA pattern over the tropical Pacific. To quantitatively depict this signal, a third predictor, named TPSST, was defined as the difference between the sum of the averaged SSTs in two positive correlation boxes and the averaged SSTs in the negative correlation box (positive domain minus negative domain).

The time series shown in Fig.1b indicates that a strong SFRI event often occurs after a peak El Niño, such as in 1983, 1992, 1995, 1998, 2005, and 2010. The predictor TPSST reflects SSTA during a decaying ENSO that sets up favorable conditions for persistence of the anomalous higher SLP over WNP. The western Pacific warming and the cooling to its east imply an enhancement of higher pressure (anticyclone) over WNP (Wang *et al*., 2000). Numerical experiments have shown that the positive thermodynamic feedback between the Philippine Sea anticyclonic anomaly and the underlying Indo-WP SST dipole anomalies can maintain both the anomalous anticyclone and the SST dipole through early summer (Lau *et al*., 2004; Wang *et al*., 2013). Thus, the TPSST is a precursor for the enhanced WPSH during MJ. This predictor was consistent with the predictor ‘JFMA EQSST’ used in MJ EA rainfall pattern prediction (Xing *et al*., 2017), except for the different lead time. The physical mechanisms behind the precursor’s effect on MJ SFR were also consistent. Therefore, only a brief explanation is given in this study. For more information, please refer to Xing *et al*. (2017).

5 A P-E Prediction Model for MJ Subtropical Frontal Rainfall

Based on the discussion in Section 4, three physical predictors have been identified: ARCSIC, EUASLP, and TPSST. The precise definition of each predictor is presented in Table 1. The CCs of ARCSIC, EUASLP, and TPSST, as they relate to SFRI, were 0.58, 0.40, and 0.45, respectively, which are all statistically significant at the

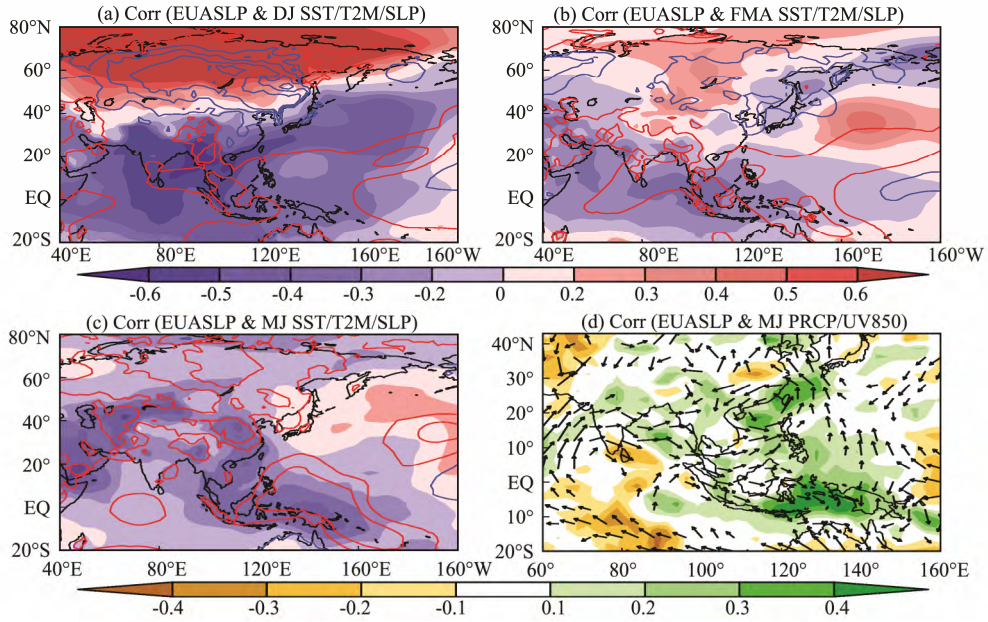

Fig.6 Correlation maps of (a) DJ mean; (b) FMA mean; and (c) MJ mean SLP (shading), SST (contours over ocean) and 2 m air temperature (contours over land) based on the predictor EUASLP. Red solid contours indicate a positive correlation coefficient between SST/T2M and EUASLP starting from 0.2 with an interval of 0.2. A similar interval applies to the blue line, except for a negative correlation. (d) Same as in (c) but for MJ mean precipitation (shading) and 850 hPa winds (vectors).

95% confidence level based on a Student's *t* test (Table 2). The CCs among the predictors are also summarized in Table 2. All predictors were highly independent of each other.

Table 2 Correlation coefficients with predict and predictors for the period 1979–2016

	SFRI	ARCSIC	EUASLP	TPSST
ARCSIC	0.58	1.0	0.28	0.14
EUASLP	0.40	–	1.0	0.02
TPSST	0.45	–	–	1.0

To estimate the MJ SFR prediction, we developed a P-E prediction model using the predictors shown in Table 1. Due to their relative independence, all three predictors were selected by stepwise regression and given the *F*-test at the 95% confidence level. The prediction (simulation) equation used was

$$SFRI = 0.45 \times ARCSIC + 0.27 \times EUASLP + 0.39 \times TPSST \,. \quad (1)$$

All predictors involved information before or during the preceding January, hence this model was a 3-month lead prediction model. The correlation between the simulation and the observation of the SFRI was 0.78. Among the above precursors, the abnormal ASI had the largest contribution to SFRI variability, implying that ASI may be a valuable predictor for long-lead seasonal prediction of climate variation over EA in summer.

To test the predictive capability of the P-E model, a cross-validation (Michaelsen, 1987) was performed to hindcast the SFRI (1979–2016). To prevent an overfitting problem, we chose a leaving-three-out strategy (10% of the whole hindcast period). The relevant procedures were as follows: the cross-validation method systematically deleted three years from the period 1979–2016, derived a forecast model from the remaining years, and tested it on the deleted cases. The cross-validated estimates of the SFRI are shown in Fig.7. The CC between the observation (black line in Fig.7) and the 38-year cross-validated estimates of the P-E model (red line in Fig.7) was 0.72.

To confirm whether the P-E model is practically useful, we used 1979–2006 data as a training period to derive a prediction equation, and then made independent forecasts for the period 2007–2016 (green line in Fig.7). The independent forecast CC skill was 0.69. This independent test could rigorously reflect the ability of the P-E prediction model in the SFRI forecast. The high skill of the independent forecast indicated that the P-E model can be used to make real time forecasts.

If we established the prediction model without the ARCSIC and performed the same hindcast, the CC between the observation and the 38-year cross-validated estimates would have been 0.49 (blue line in Fig.7). This indicates that the ASI anomaly does significantly improve the seasonal prediction skill of the P-E model.

To assess the performance of the rainfall prediction by numerical models, we used retrospective forecasts of four advanced atmosphere-ocean coupled models with initial conditions in early May from 1979 to 2010, including the National Center for Environmental Prediction (NCEP) CFS version 2 (Saha *et al.*, 2014), the Australia Bureau of Meteorology (ABOM) POAMA version 2.4 (Hudson *et al.*, 2011), the Geophysical Fluid Dynamics Laboratory (GFDL) CM version 2.1 (Delworth *et al.*, 2006), and the Frontier Research Center for Global Change (FRCGC) SINTEX-F model (Luo *et al.*, 2005). It has been generally recognized that multi-model ensemble (MME) prediction has con-

siderably higher skill than individual model prediction (Lee *et al*., 2010). To obtain higher skill, we used the MME prediction by simply averaging the four coupled models' ensemble mean anomalies after removing their own climatology. The CC between the observation and the 32-year MME hindcast was only 0.47. The MME hindcast skill was lower than the P-E model prediction skill, implying the advantage of the P-E model in seasonal prediction of subtropical climate variability.

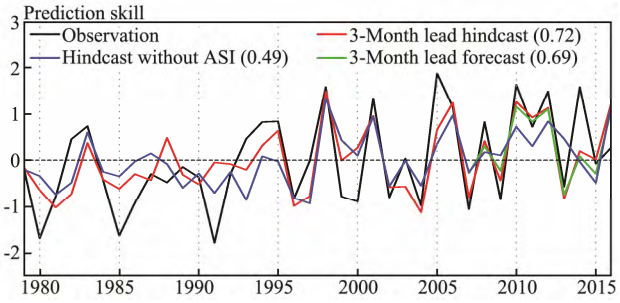

Fig.7 Prediction skill for the physical-empirical prediction shown by the time series of observation (black) and cross-validated predictions using three 3-month lead predictors (red) over 38 years. The cross validation was done by taking three years out from around the predicted year. The cross-validated correlation skill was 0.72. The 2007–2016 values (green) are independent test predictions, which had a forecast temporal correlation skill of 0.69 when the model was built using data in the training period of 1979–2006. The hindcasted time series without Arctic sea ice signals is also shown by the blue line for comparison.

6 Conclusions

EA subtropical frontal rainfall (SFR) is a defining feature of the Asian monsoon. Prediction of MJ mean EA SFR is of central importance as it affects a large number of populations. The present study aimed to predict MJ EA SFR at a longer-lead time using ASI anomalies as a potential predictor as well as the climate systems originating from the tropics to the mid-latitudes for the 38-year period of 1979–2016.

In order to measure the strength of the MJ SFR, an SFRI was defined using the leading PC of an EOF analysis applied to MJ rainfall anomalies over EA. This index presents an enhancement of the climatological MJ mean rain band stretching from southern China to south of Japan. Enhancement of the WPSH and the Okhotsk High and anomalous lower sea level pressure (SLP) over eastern China are featured circulation anomalies that have close relationships with a strong MJ SFRI.

Based on their circulation characteristics, three physical precursors from the preceding autumn and winter have been identified. The first precursor (ARCSIC) is a dipolar SIC anomaly in the Arctic during the preceding autumn (October–November mean, ON), which signifies a negative NAO and tripole SSTA over the northern Atlantic that can persist until early summer. The tripole SSTA may excite downstream development of subpolar teleconnections, raising the pressure over the Okhotsk Sea. The second precursor is a dipolar SLP anomaly during the preceding winter (DJ) over northern Eurasia and EA (EUASLP), which interacts with warming SSTs in the warm pool region and leads to a persistent lower SLP over EA. This favors enhanced local rainfall during early summer. The third predictor is the tripole SSTA in the tropical Pacific in DJ (TPSST), which signifies enhancement of WPSH, which, in turn, can persist until early summer through anticyclone-SST dipole interaction.

On the basis of the dynamical processes, a physical-empirical (P-E) model was established to predict the MJ SFRI by combining the three predictors. All predictors involved information before or during the preceding January, thus this model is a 3-month lead prediction model. Cross-validated hindcasting was performed for the 1979–2016 period. The CC skill reached 0.72, which showed a notably higher prediction skill than the MME hindcast of four state-of-the-art models (0.47). It suggests that the predictive power of the current dynamical models leaves much room to improve.

Although previous studies have indicated that long-lead seasonal prediction would be difficult and skills would decrease as lead time increased, the present 3-month lead hindcast skill using ASI as a new predictor was comparable to that of the 0-month lead prediction model established by Xing *et al*. (2017), both being 0.72. By examining the normalized regression coefficient of the P-E model, we could directly compare the relative contribution of each predictor. Among the above three precursors, ARCSIC had the largest contribution to the long-lead prediction. Furthermore, the cross-validated hindcast CC skill decreased sharply to 0.49 without the ASI predictor. These results all indicate that the ASI anomaly does significantly improve the seasonal prediction skill of the P-E model, and that it is a valuable predictor, especially in terms of long-lead prediction.

In a previous study, we had established a P-E model for MJ southern China rainfall prediction at a 2-month lead time for the period of 1979–2012 (Yim *et al*., 2014). The SFRI index in our work, however, offers a detailed spatial structure of the rainfall anomalies. Furthermore, the present work pays more attention to the contribution of ASI on EA climate variation. A longer-lead time prediction is established involving anomalous Arctic climate, and the targeting period expands to 2016.

Understanding the physical linkages between predictands and predictors is crucial for selecting predictors and improving prediction skills. The principles of searching for relatively independent and complimentary predictors should be useful for a reduction in predictive skill drop (Wang *et al*., 2015). While the causative processes linking the predictors and the SFRI have been speculated, they are, by no means, rigorous proofs; thus, further, well-designed numerical experiments with credible climate models are needed to validate or refute the mechanism proposed in the present study.

Acknowledgements

The work was supported by the Global Change Research

Program of China (No. 2015CB953904), and the National Natural Science Foundation of China (No. 41575067).

References

Alexander, M. A., Bhatt, U. S., Walsh, J. E., Timlin, M. S., Miller, J. S., and Scott, J. D., 2004. The atmospheric response to realistic Arctic sea ice anomalies in an AGCM during winter. *Journal of Climate*, **17** (5): 890-905.

Chen, G. T. J., 1983. Observational aspects of the Meiyu phenomena in subtropical China. *Journal of Meteorological Society of Japan*, **61**: 306-312.

Dee, D. P., Uppala, S. M., Simmons, A. J., Berrisford, P., Poli, P., Kobayashi, S., Andrae, U., Balmaseda, M. A., Balsamo, G., Bauer, D. P., and Bechtold, P., 2011. The ERA–Interim reanalysis: Configuration and performance of the data assimilation system. *Quarterly Journal of the Royal Meteorological Society*, **137** (656): 553-597.

Delworth, T. L., Broccoli, A. J., Rosati, A., Stouffer, R. J., Balaji, V., Beesley, J. A., Cooke, W. F., Dixon, K. W., Dunne, J., Dunne, K. A., and Durachta, J. W., 2006. GFDL's CM2 global coupled climate models. Part I: Formulation and simulation characteristics. *Journal of Climate*, **19** (5): 643-674.

Deser, C., Magnusdottir, G., Saravanan, R., and Phillips, A., 2004. The effects of North Atlantic SST and sea ice anomalies on the winter circulation in CCM3. Part II: Direct and indirect components of the response. *Journal of Climate*, **17** (5): 877-889.

Deser, C., Tomas, R., Alexander, M., and Lawrence, D., 2010. The seasonal atmospheric response to projected Arctic sea ice loss in the late twenty-first century. *Journal of Climate*, **23** (2): 333-351.

Ding, Y., 1992. Summer monsoon rainfalls in China. *Journal of the Meteorological Society of Japan*, **70** (1B): 373-396.

Gu, W., Li, C., Li, W., Zhou, W., and Chan, J. C., 2009a. Interdecadal unstationary relationship between NAO and East China's summer precipitation patterns. *Geophysical Research Letters*, **36** (13): L13702.

Gu, W., Li, C., Wang, X., Zhou, W., and Li, W., 2009b. Linkage between mei-yu precipitation and North Atlantic SST on the decadal timescale. *Advances in Atmospheric Sciences*, **26** (1): 101-108.

Holland, M. M., Bitz, C. M., and Tremblay, B., 2006. Future abrupt reductions in the summer Arctic sea ice. *Geophysical Research Letters*, **33** (23): L32503.

Honda, M., Inoue, J., and Yamane, S., 2009. Influence of low Arctic sea-ice minima on anomalously cold Eurasian winters. *Geophysical Research Letters*, **36** (8): L08707.

Huang, B., Banzon, V. F., Freeman, E., Lawrimore, J., Liu, W., Peterson, T. C., Smith, T. M., Thorne, P. W., Woodruff, S. D., and Zhang, H. M., 2015. Extended reconstructed sea surface temperature version 4 (ERSST. v4). Part I: Upgrades and intercomparisons. *Journal of Climate*, **28** (3): 911-930.

Hudson, D., Alves, O., Hendon, H. H., and Wang, G., 2011. The impact of atmospheric initialisation on seasonal prediction of tropical Pacific SST. *Climate Dynamics*, **36** (5-6): 1155-1171.

Huffman, G. J., Bolvin, D. T., and Adler, R. F., 2011. Last updated GPCP Version 2.2 combined precipitation data set. WDC-A, NCDC, Asheville, NC (2011). Dataset accessed at http://www.ncdc.noaa.gov/oa/wmo/wdcamet-ncdc.html.

Kumar, A., Perlwitz, J., Eischeid, J., Quan, X., Xu, T., Zhang, T., Hoerling, M., Jha, B., and Wang, W., 2010. Contribution of sea ice loss to Arctic amplification. *Geophysical Research Letters*, **37** (21): L21701.

Lau, N. C., Nath, M. J., and Wang, H., 2004. Simulations by a GFDL GCM of ENSO-related variability of the coupled atmosphere-ocean system in the East Asian monsoon region. In: *East Asian Monsoon, World Scientific Series on Meteorology of East Asia* No. 2. Chang, C. P., ed., World Scientific, Singapore, 271-300.

Lee, J. Y., Lee, S. S., Wang, B., Ha, K. J., and Jhun, J. G., 2013. Seasonal prediction and predictability of the Asian winter temperature variability. *Climate Dynamics*, **41** (3-4): 573-587.

Lee, J. Y., Wang, B., Kang, I. S., Shukla, J., Kumar, A., Kug, J. S., Schemm, J. K. E., Luo, J. J., Yamagata, T., Fu, X., and Alves, O., 2010. How are seasonal prediction skills related to models' performance on mean state and annual cycle? *Climate Dynamics*, **35** (2-3): 267-283.

Lee, S. S., Lee, J. Y., Ha, K. J., Wang, B., and Schemm, J. K. E., 2011. Deficiencies and possibilities for long-lead coupled climate prediction of the Western North Pacific-East Asian summer monsoon. *Climate Dynamics*, **36** (5-6): 1173-1188.

Li, B., and Zhou, T., 2011. ENSO-related principal interannual variability modes of early and late summer rainfall over East Asia in SST-driven AGCM simulations. *Journal of Geophysical Research*, **116**: 1-15.

Li, J., and Wang, J. X., 2003a. A modified zonal index and its physical sense. *Geophysical Research Letters*, **30** (12): 1632.

Li, J., and Wang, J. X., 2003b. A new North Atlantic Oscillation index and its variability. *Advances in Atmospheric Sciences*, **20** (5): 661-676.

Li, J., and Wu, Z., 2012. Importance of autumn Arctic sea ice to northern winter snowfall. *Proceedings of the National Academy of Sciences*, **109** (28): E1898-E1898.

Li, J., and Wang, B., 2016. How predictable is the anomaly pattern of the Indian summer rainfall? *Climate Dynamics*, **46** (9-10): 2847-2861.

Liu, J., Curry, J. A., Wang, H., Song, M., and Horton, R. M., 2012. Impact of declining Arctic sea ice on winter snowfall. *Proceedings of the National Academy of Sciences*, **109** (11): 4074-4079.

Liu, W., Huang, B., Thorne, P. W., Banzon, V. F., Zhang, H. M., Freeman, E., Lawrimore, J., Peterson, T. C., Smith, T. M., and Woodruff, S. D., 2015. Extended reconstructed sea surface temperature version 4 (ERSST. v4): Part II. Parametric and structural uncertainty estimations. *Journal of Climate*, **28** (3): 931-951.

Luo, J. J., Masson, S., Behera, S., Shingu, S., and Yamagata, T., 2005. Seasonal climate predictability in a coupled OAGCM using a different approach for ensemble forecasts. *Journal of climate*, **18** (21): 4474-4497.

Magnusdottir, G., Deser, C., and Saravanan, R., 2004. The effects of North Atlantic SST and sea ice anomalies on the winter circulation in CCM3. Part I: Main features and storm track characteristics of the response. *Journal of Climate*, **17** (5): 857-876.

Michaelsen, J., 1987. Cross-validation in statistical climate forecast models. *Journal of Climate and Applied Meteorology*, **26** (11): 1589-1600.

North, G. R., Bell, T. L., Cahalan, R. F., and Moeng, F. J., 1982. Sampling errors in the estimation of empirical orthogonal functions. *Monthly Weather Review*, **110** (7): 699-706.

Oh, H., and Ha, K. J., 2015. Thermodynamic characteristics and responses to ENSO of dominant intraseasonal modes in the East Asian summer monsoon. *Climate Dynamics*, **44** (7-8): 1751-1766.

Panofsky, H. A., and Brier, G. W., 1968. *Some Applications of Statistics to Meteorology*. Pennsylvania State University Press, University Park, PA, 1-224.

Rayner, N. A. A., Parker, D. E., Horton, E. B., Folland, C. K., Alexander, L. V., Rowell, D. P., Kent, E. C., and Kaplan, A., 2003. Global analyses of sea surface temperature, sea ice, and night marine air temperature since the late nineteenth century. *Journal of Geophysical Research: Atmospheres*, **108** (D14): 4407.

Saha, S., Moorthi, S., Wu, X., Wang, J., Nadiga, S., Tripp, P., Behringer, D., Hou, Y. T., Chuang, H. Y., Iredell, M., and Ek, M., 2014. The NCEP climate forecast system version 2. *Journal of Climate*, **27** (6): 2185-2208.

Serreze, M. C., Holland, M. M., and Stroeve, J., 2007. Perspectives on the Arctic's shrinking sea-ice cover. *Science*, **315** (5818): 1533-1536.

Singarayer, J. S., Bamber, J. L., and Valdes, P. J., 2006. Twenty-first-century climate impacts from a declining Arctic sea ice cover. *Journal of Climate*, **19** (7): 1109-1125.

Su, Q., Lu, R., and Li, C., 2014. Large-scale circulation anomalies associated with interannual variation in monthly rainfall over South China from May to August. *Advances in Atmospheric Sciences*, **31** (2): 273-282.

Tao, S. Y., and Chen, L., 1987. A review of recent research on the East Asian summer monsoon in China. In: *Monsoon Meteorology*. Chang, C. P., and Krisnamurti, T. N., eds., Oxford University Press, Oxford, 60-92.

Wang, B., and Ho, L., 2002. Rainy season of the Asian-Pacific summer monsoon. *Journal of Climate*, **15** (4): 386-398.

Wang, B., Lee, J. Y., and Xiang, B., 2015a. Asian summer monsoon rainfall predictability: A predictable mode analysis. *Climate Dynamics*, **44** (1-2): 61-74.

Wang, B., Lee, J. Y., Kang, I. S., Shukla, J., Kug, J. S., Kumar, A., Schemm, J., Luo, J. J., Yamagata, T., and Park, C. K., 2008. How accurately do coupled climate models predict the leading modes of Asian-Australian monsoon interannual variability? *Climate Dynamics*, **30** (6): 605-619.

Wang, B., Liu, J., Yang, J., Zhou, T., and Wu, Z., 2009. Distinct principal modes of early and late summer rainfall anomalies in East Asia. *Journal of Climate*, **22** (13): 3864-3875.

Wang, B., Wu, R., and Fu, X., 2000. Pacific-East Asian teleconnection: How does ENSO affect East Asian climate? *Journal of Climate*, **13** (9): 1517-1536.

Wang, B., Wu, R., and Lau, K. M., 2001. Interannual variability of the Asian summer monsoon: Contrasts between the Indian and the western North Pacific-East Asian monsoons. *Journal of Climate*, **14** (20): 4073-4090.

Wang, B., Xiang, B., and Lee, J. Y., 2013. Subtropical high predictability establishes a promising way for monsoon and tropical storm predictions. *Proceedings of the National Academy of Sciences*, **110** (8): 2718-2722.

Wang, B., Xiang, B., Li, J., Webster, P. J., Rajeevan, M. N., Liu, J., and Ha, K. J., 2015b. Rethinking Indian monsoon rainfall prediction in the context of recent global warming. *Nature Communications*, **6**: 7154.

Wang, M., and Overland, J. E., 2009. A sea ice free summer Arctic within 30 years? *Geophysical Research Letters*, **36** (7): L07 502.

Wu, B., Su, J., and Zhang, R., 2011. Effects of autumn–winter Arctic sea ice on winter Siberian High. *Chinese Science Bulletin*, **56** (30): 3220-3228.

Wu, B., Zhang, R., Wang, B., and D'Arrigo, R., 2009a. On the association between spring Arctic sea ice concentration and Chinese summer rainfall. *Geophysical Research Letters*, **36** (9): L09501.

Wu, R., and Wang, B., 2002. A contrast of the East Asian summer monsoon – ENSO relationship between 1962–77 and 1978–93. *Journal of Climate*, **15** (22): 3266-3279.

Wu, Z., Li, J., Jiang, Z., and He, J., 2011. Predictable climate dynamics of abnormal East Asian winter monsoon: Once-in-a-century snowstorms in 2007/2008 winter. *Climate Dynamics*, **37** (7-8): 1661-1669.

Wu, Z., Li, X., Li, Y., and Li, Y., 2016. Potential influence of Arctic sea ice to the interannual variations of East Asian spring precipitation. *Journal of Climate*, **29** (8): 2797-2813.

Wu, Z., Wang, B., Li, J., and Jin, F. F., 2009b. An empirical seasonal prediction model of the East Asian summer monsoon using ENSO and NAO. *Journal of Geophysical Research: Atmospheres*, **114** (D18): D18120.

Xing, W., and Wang, B., 2017. Predictability and prediction of summer rainfall in the arid and semi-arid regions of China. *Climate Dynamics*, **49** (1-2): 419-431.

Xing, W., Wang, B., and Yim, S. Y., 2016. Peak-summer East Asian rainfall predictability and prediction part I: Southeast Asia. *Climate Dynamics*, **47** (1-2): 1-13.

Xing, W., Wang, B., Yim, S. Y., and Ha, K. J., 2017. Predictable patterns of the May–June rainfall anomaly over East Asia. *Journal of Geophysical Research: Atmospheres*, **122** (4): 2203-2217.

Yim, S. Y., Wang, B., and Xing, W., 2014. Prediction of early summer rainfall over South China by a physical-empirical model. *Climate Dynamics*, **43** (7-8): 1883-1891.

Yim, S. Y., Wang, B., and Xing, W., 2016. Peak-summer East Asian rainfall predictability and prediction part II: Extratropical East Asia. *Climate Dynamics*, **47** (1-2): 15-30.

Yuan, Y., Yang, H., Zhou, W., and Li, C., 2008a. Influences of the Indian Ocean Dipole on the Asian summer monsoon in the following year. *International Journal of Climatology*, **28** (14): 1849-1859.

Yuan, Y., Zhou, W., Chan, J. C., and Li, C., 2008b. Impacts of the basin-wide Indian Ocean SSTA on the South China Sea summer monsoon onset. *International Journal of Climatology*, **28** (12): 1579-1587.

Yun, K. S., Seo, K. H., and Ha, K. J., 2010. Interdecadal change in the relationship between ENSO and the intraseasonal oscillation in East Asia. *Journal of Climate*, **23** (13): 3599-3612.

Zhang, L., and Li, T., 2017. Physical processes responsible for the interannual variability of sea ice concentration in Arctic in boreal autumn since 1979. *Journal of Meteorological Research*, **31** (3): 468-475.

Zhou, T., Gong, D., Li, J., and Li, B., 2009. Detecting and understanding the multi-decadal variability of the East Asian Summer Monsoon – Recent progress and state of affairs. *Meteorologische Zeitschrift*, **18** (4): 455-467.

Zuo, J., Ren, H. L., Wu, B., and Li, W., 2016. Predictability of winter temperature in China from previous autumn Arctic sea ice. *Climate Dynamics*, **47** (7-8): 2331-2343.

(Edited by Chen Wenwen)